Passive Flexibility Effect on Oscillating Foil Energy Harvester

Wendi Liu* and Qing Xiao†
University of Strathclyde, Glasgow, Scotland G4 0LZ, United Kingdom
and
Qiang Zhu‡
University of California, San Diego, La Jolla, California 92093

DOI: 10.2514/1.J054205

It is well known that structural flexibility enhances the performance of flapping foil propellers. There is, however, much less knowledge about the effect of deformability on the flow energy extraction capacity of flapping foils. Following recent work on an oscillating foil energy harvesting device with prescribed foil deformations (Liu et al., "A Bio-Inspired Study on Tidal Energy Extraction with Flexible Flapping Wings," Bioinspiration and Biomimetics, Vol. 8, No. 3, 2013, Paper 036011), fully coupled dynamics of a flapping foil energy harvester with a passively deformable foil is investigated. Toward this end, the dynamics of a foil with a realistic internal structure (containing a rigid leading edge and a flexible trailing edge with a stiffener) in an energy harvesting regime through a fluid–structure interaction scheme is computationally studied. To examine the effect of different levels of flexibility, various materials (ranging from metals such as copper to virtual materials with arbitrary elasticity and density) for the stiffener have been tested. With the virtual materials, the effects of Young's modulus and density ratio have been studied. The simulation results show that flexibility around the trailing edge could enhance the overall energy extraction performance. For example, with a copper stiffener, an increase of 32.2% in efficiency can be reached at high reduced frequency. The performance enhancement is achieved mostly in cases with low Young's modulus and density ratio. A possible underlying mechanism is that the specific foil deformations in these cases encourage the generation and shedding of vortices from the foil leading edge, which is known to be beneficial to flow energy extraction.

Nomenclature

A	=	sweep area, m^2
$\mathcal{AR}$ 2	=	aspect ratio
$C_L(t)$	=	instantaneous lift coefficient
C_{op}	=	power coefficient
c	=	chord length, m
c_{pit}	=	pitching center, m
c_{sf}	=	length of metal stiffener, m
E	=	Young's modulus, Pa
E_c	=	Young's modulus coefficient
f_n	=	natural frequency of selected material, Hz
f_0	=	frequency of flapping wing, Hz
$f_{0.18}$	=	frequency of flapping wing under f^* equal to 0.18, Hz
f^*	=	reduced frequency
g	=	gravitational acceleration, m/s^2
$h(t)$	=	instantaneous heaving position, m
h_0	=	amplitude of heaving motion, m
L	=	lift force, N
M	=	moment, Nm
$M_Z(t)$	=	instantaneous moment coefficient
p	=	instantaneous power, W
Re	=	Reynolds number
St	=	Strouhal number of foil oscillating
T	=	oscillating period, s
T_{sf}	=	thickness of metal stiffener, m
t	=	instant time, s
U_∞	=	freestream velocity, m/s
β_0	=	instantaneous nondimensional trailing-edge bending distance normalized by chord length relative to local coordinates
β_{0amp}	=	amplitude of nondimensional trailing-edge bending distance normalized by chord length relative to local coordinates
η	=	energy extraction efficiency
θ_0	=	amplitude of pitching motion, deg
$\theta(t)$	=	instantaneous pitching angle, deg
ν	=	Poisson ratio
Π	=	effective stiffness
ρ_f	=	density of fluid, kg/m^3
ρ_s	=	density of structure, kg/m^3
φ	=	phase difference between heave and pitch motion, rad

Received 9 February 2015; revision received 20 May 2015; accepted for publication 17 June 2015; published online 7 January 2016.

*Ph.D. Student, Department of Naval Architecture, Ocean and Marine Engineering.

†Senior Lecturer, Department of Naval Architecture, Ocean and Marine Engineering; qing.xiao@strath.ac.uk. Senior Member AIAA (Corresponding Author).

‡Associate Professor, Department of Structural Engineering.

I. Introduction

MOST of the existing tidal current renewable energy devices can be classified into three groups (i.e., horizontal axis turbine, vertical axis turbine, and oscillating foil turbine). The bioinspired tidal energy harvester, an oscillating foil turbine imitating the fish fins or insect wings and utilizing their flapping motions to extract energy from their surrounded fluid, is one of the most novel devices. Compared with the traditional rotating turbine, oscillating foil turbines present several distinguishing characteristics, such as its suitableness in shallow water, mitigation of centrifugal force/stress, and low noise during its operation [1]. Because of the initial development of McKinney and DeLaurier [2], in the past few years, oscillating foil turbines have been extensively studied because of the growing interest in biomimetics and the improved knowledge about unsteady fluid dynamics involved in flying and swimming motions [3]. The studies about flapping foil energy harvesters fall into three categories: fully activated systems with prescribed motions, semi-activated systems with one degree-of-freedom activated and another one induced by fluid dynamic loads, and fully passive systems in which the motions are completely generated by flow-induced instability (i.e., flutter phenomenon) as stated in a recent review paper by Xiao and Zhu [1]. Among these, the fully activated systems are usually used as model systems. By assuming that the foil undergoes certain

prescribed motions (in reality, these motions can be generated either semi-actively or passively), these model systems are useful in examining the power extraction capacity of the system and the underlying physics. Because the research about flapping foil energy harvesters is still at the beginning stage, most of the existing studies use prescribed foil motions [1]. However, most existing investigations are limited to rigid oscillating foils [4–10].

In nature, many animals deform their bodies or fins either actively or passively to achieve higher thrust efficiency or to generate larger transient forces for maneuvering and stabilizing purposes. Insect wings, such as butterfly or bee wings, can generate asymmetric forces by their twisting and bending motions to achieve high time-averaged forces [11]. Combes and Daniel [12,13] presented a three-dimensional investigation on the stiffness distribution of insect wings in both chordwise and spanwise directions. They observed that the wing stiffness in the spanwise direction is higher than that in the chordwise direction. A sharply decreasing flexural stiffness is observed from the wing base to the leading edge, when a large bending moment is applied. Investigations by Zhu [14] indicated that the chordwise flexibility could enhance the propulsion efficiency of the wing. Shoele and Zhu [15] numerically studied propulsion by flexible ray fins. Similar to insect wings, ray fins have enhanced stiffness around their leading edges, making it easier to control the local angle of attack (AOA) to mitigate leading-edge vortices (LEVs) formation and shedding. With flexible fin motion, ray fins can significantly reduce the leading-edge AOA to enhance propulsion efficiency. On the other hand, when an insect wing is used for lift generation, its strengthened leading edge helps with stabilizing and enhancing the LEV and improves its force-generation performance [16]. In fact, it is generally accepted that LEV enhancement is the key mechanism to obtain higher lift force for a flapping wing system at Reynolds numbers up to 10^4 [17].

Associated with the flexible features of flapping wings, the system inertia is also found to play a role on the force-generation performance. Daniel and Combes [18] investigated the inertia effect of flexible insect wings in air (also see [19]), which has usually been ignored by previous researchers. Their results indicated that inertia played a primary role in the wing deformation. Zhu [14] investigated the density ratio effect on flapping foil performance by taking the inertia and structure dissipation into account. Two different densities of surrounding media were studied (i.e., air and water). It is found that the structure inertia determines the level of deformation when surrounding media has low density, whereas the fluid load dominates the deformation when the surrounding media has high density. The propulsion efficiency decreases with foil flexibility in a low-density medium. However, it increases with flexibility in high-density fluid.

In contrast to the numerous investigations about the effects of structural deformability on the force-generation performance of flapping foils, the energy harvesting capacity of flexible flapping foils has not been well understood. In our previous study [20], a two-dimensional oscillating foil at $Re = 1.0 \times 10^6$ was examined by using a Navier–Stokes solver under turbulent flow conditions. In that study, the deformation of the foil was prespecified. According to that study, leading-edge flexibility may lead to earlier shedding of LEVs, resulting in changes in phase of the instantaneous forces and moments. Subsequently, a 7.68% increment in energy extraction efficiency is observed when the effective AOA is 10 deg. This, however, can only be achieved under certain foil deformations that have to be created through active controlling.

In a recent work by Tian et al. [21], a fluid–structure interaction model with an immersed-boundary method was used to study the flow energy extraction by a flexible plate. Four systems were investigated: rigid plate, flexible plate, flexible leading segment with rigid trailing segment, and rigid plate with active control of the leading segment. Their results show an 11.3% enhancement of energy extraction efficiency by applying active control to the leading-edge segment. However, for a passively flexible plate, no performance enhancement was observed.

In the present study, we examine the energy extraction of a passively flexible flapping foil through a fully coupled fluid–structure interaction study. Unlike the simplified plate model with zero thickness [21], a more realistic NACA 0012 foil shape is used in the present study. In addition, we take into account the internal structure of the foil by using a stiffener to create the structural deformability. This makes our model closer to the real design. In this study, a finite volume method is used, which fully resolves the boundary layer so that it has better accuracy than the immersed-boundary method.

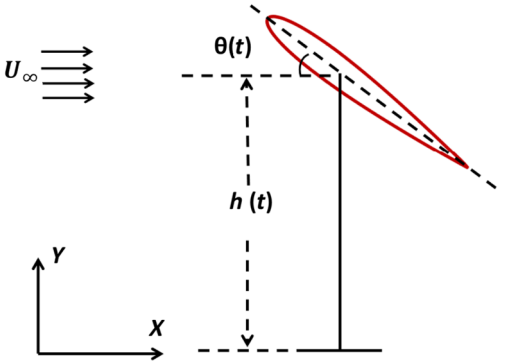

Fig. 1 Schematic diagram for oscillating energy device.

In the rest of the paper, descriptions of the physical problem and the corresponding numerical methods are listed in Sec. II. In Sec. III, we first consider cases with a metal stiffener to examine whether structural flexibility has a beneficial effect on energy extraction. The effects of Young's modulus coefficient and density ratio are then studied separately. Finally, conclusions of these studies are listed in Sec. IV.

II. Problem Formulation and Numerical Methodology

A. Problem Description

The present research considers a two-dimensional oscillating energy harvesting system based on a NACA 0012 foil, whose deformability is determined by a realistic internal structure. As shown in Fig. 1, the incoming flow is uniform with speed U_∞. Similar to the study by Kinsey and Dumas [4], the Reynolds number based on the incoming flow speed and the chord length c of the foil in the current study is fixed as 10^3 so that a laminar flow assumption is used. In applications, there exist three types of design [1]: systems with forced pitching and heaving motions, systems with forced pitching and induced heaving motions (semi-activated systems), and systems with self-sustained pitching and heaving motions (self-sustained systems). In the current study, we concentrate on the first type [2,4–6,22,23] and examine the effects of structural flexibility upon the energy harvesting performance.

1. *Kinematics*

As demonstrated in Fig. 1, the kinematics of the foil includes the pitch and heave motions specified as

$$h(t) = h_0 \sin(2\pi f_0 t) \tag{1}$$

$$\theta(t) = \theta_0 \sin(2\pi f_0 t + \varphi) \tag{2}$$

where $h(t)$ and $\theta(t)$ are the instantaneous heave and pitch motions with the amplitudes of h_0 and θ_0, respectively; f_0 is the oscillating frequency of the foil; and φ, which has a fixed value of $-\pi/2$ during the current research, is the phase difference between heave and pitch motions. The pitch axis is located at one-quarter chord length from the leading edge of the foil (i.e., $c_{\text{pit}}/c = 1/4$).

Following the study of Kinsey and Dumas [5], the heave amplitude is chosen to be one chord length ($h_0/c = 1$). Two pitching amplitudes, 60 and 73 deg, are examined.

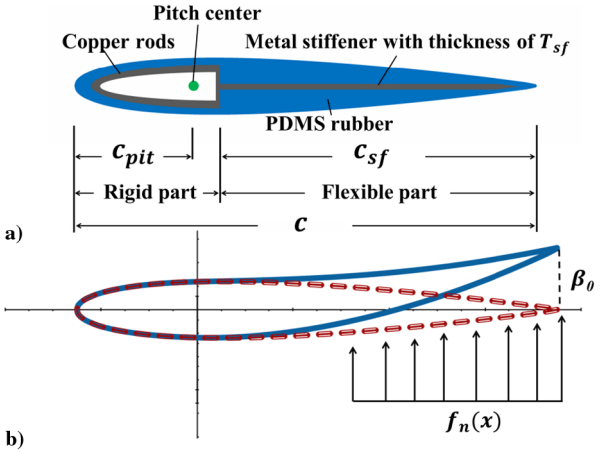

Fig. 2 Flexible foil a) inner structural design for trailing edge and b) displacement.

The oscillating frequency is usually characterized by the reduced frequency f^* defined as

$$f^* = \frac{f_0 c}{U_\infty} \tag{3}$$

2. *Energy Extraction Performance*

The key parameters to quantify the energy extraction performance of an oscillating foil system are the nondimensional instantaneous power coefficient C_{op} and the total energy extraction efficiency η. They are determined by

$$C_{\text{op}} = \frac{p}{\frac{1}{2}\rho_f U_\infty^3 c} = \frac{1}{U_\infty}\left[C_L(t)\frac{\mathrm{d}h(t)}{\mathrm{d}t} + cM_Z(t)\frac{\mathrm{d}\theta(t)}{\mathrm{d}t}\right] \tag{4}$$

and

$$\eta = \frac{\bar{p}}{\frac{1}{2}\rho_f U_\infty^3 A} = \overline{C_{\text{op}}}\frac{c}{A} \tag{5}$$

where p is the instantaneous power with a time-averaged value of $\bar{p}$, ρ_f is the fluid density, and A is the sweep area of the oscillating wing. $C_L(t)$ and $C_m(t)$ are the instantaneous lift and moment coefficient defined as

$$C_L(t) = \frac{L}{\frac{1}{2}\rho_f U_\infty^2 c} \tag{6}$$

$$M_Z(t) = \frac{M}{\frac{1}{2}\rho_f U_\infty^2 c^2} \tag{7}$$

where L is the lift force and M is the moment of the foil.

3. *Structural Design of Flexible Foils*

To study the effect of structural deformability on the propulsion performance of a flapping wing, Heathcote et al. [24,25] developed chord- and spanwise flexible wing models and performed experimental tests. Subsequently, relevant numerical simulations were also carried out by Shyy et al. [17], Gordnier et al. [26], and Chimakurthi et al. [27]. In the present study, we adopt similar internal designs from the preceding papers and create a foil with chordwise flexibility (Fig. 2a). Given a NACA 0012 profile, the deformability of this foil is determined by a stiffener with thickness T_{sf} and length c_{sf}. In the present study, the stiffener thickness T_{sf} and length c_{sf} are fixed for all cases as $9 \times 10^{-3}c$ and $0.75c$, respectively. We assume that the surrounding material is light and soft so that its inertia and stiffness are negligible. Indeed, by comparing experimental and numerical results, Gordnier et al. [26,28] and Chimakurthi et al. [27] concluded that the surrounding material (in their case, it was polydimethylsiloxane rubber (PDMS) with Young's modulus of 250 kPa [25]) contributes little to the overall structural behavior of the foil. This is partly attributed to the fact that this material tapers off near the trailing edge, where the structural deformation is most pronounced, whereas the stiffener is uniformly distributed along the chord.

With the unsteady fluid loads acting on its surface, the flexible part of the foil deforms passively, as shown in Fig. 2b. The instantaneous nondimensional trailing-edge bending distance relative to the local X coordinate (a local coordinate that coincides with the instantaneous chord of the foil if there is no deformation) is defined as $\beta_0 = \text{displacement}/c$, whose amplitude is defined as β_{0_amp}.

Young's modulus coefficient E_c and the density ratio (DR) are the two key parameters to describe the structural property. Here, they are defined as

$$\begin{cases} E_c = \frac{E}{\rho_f g c} \\ \text{DR} = \frac{\rho_s}{\rho_f} \end{cases} \tag{8}$$

where ρ_s is the density of the stiffener. The current study is focused on the flexible foil oscillating in water, thus the fluid density ρ_f we are aiming to simulate is 1000 kg/m^3.

We note that the stiffness of the structure is often characterized by the effective stiffness Π [17]. This parameter describes the elastic bending forces relative to the fluid dynamic forces as

$$\Pi = \frac{ET_{\text{sf}}^3}{12(1-v^2)\rho_f U_\infty^2 c^3} \tag{9}$$

where v is the Poisson ratio of the stiffener and c is the chord length of the foil. The effective stiffness Π was widely tested by the experiment

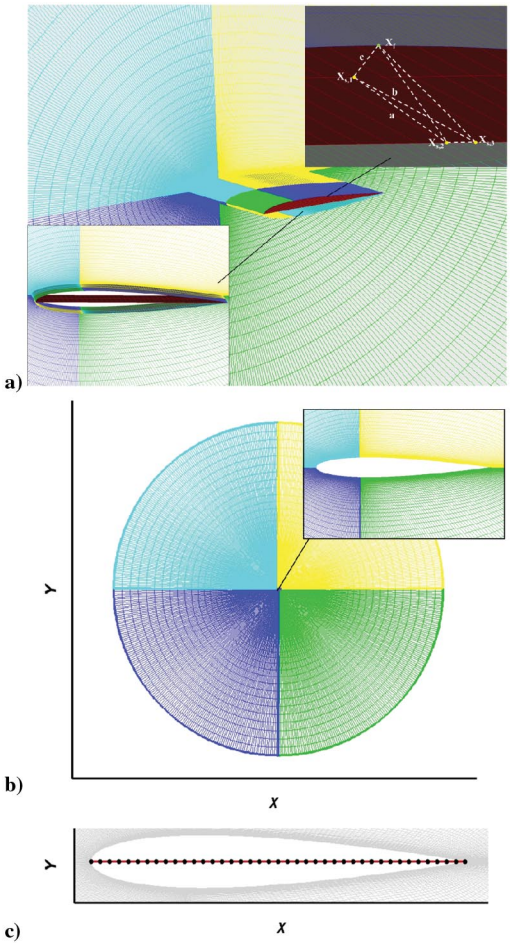

Fig. 3 Computational domain: a) 3-D view for fluid and structure meshes and corresponding CVT mapping example; b) fluid mesh in 2-D view; c) structure mesh in 2-D view.

$$\boldsymbol{f}_\mu = \begin{bmatrix} 0 & 0 & 0 \\ \tau_{xx} & \tau_{xy} & \tau_{xz} \\ \tau_{yx} & \tau_{yy} & \tau_{yz} \\ \tau_{zx} & \tau_{zy} & \tau_{zz} \\ u\tau_{xx} + v\tau_{xx} + w\tau_{xx} - q_x & u\tau_{yx} + v\tau_{yx} + w\tau_{yz} - q_y & u\tau_{zx} + v\tau_{zy} + w\tau_{zz} - q_z \end{bmatrix} \tag{14}$$

of Heathcote et al. [24,25] and numerical simulations from Chimakurthi et al. [27] and Gordnier et al. [28].

B. Mathematical Formulations and Numerical Algorithm

In this study, we apply a fluid–structure interaction model by coupling a Navier–Stokes solver with a linear structural model. High computational efficiency is achieved by the application of an implicit dual-time multigrid method for the flow, as well as a modal analysis approach for the structure. The fluid–structure coupling is achieved by subiterations. In the fluid part, a cell-centered finite volume method is used, with the numerical stability enhanced by residual smoothing. The solution of the nonlinear flow equations is accelerated by using a structured multigrid method and a parallel multiblock approach through message passing interface (MPI). A grid-deformation algorithm trans-finite interpolation is developed to interpolate the deformation of the structural boundaries onto the flow grid. Although in the current study we concentrate on a two-dimensional laminar flow problem, the in-house code we have is capable of solving three-dimensional fluid–structure interaction problems as well as flows in high Reynolds number regimes (through turbulence models such as the Baldwin–Lomax algebraic model and k-ω two equation model). The code is also capable of simulating inviscid flows with Euler equations. The detailed formulations and numerical implementation for the current study are listed in the following [20].

1. Fluid Dynamics

Our fluid solver is based on the following governing equations of unsteady laminar flow:

$$\frac{\partial}{\partial t}\int_\Omega W \,\mathrm{d}\Omega + \oint_{\partial\Omega} (f - f_\mu)\,\mathrm{d}S = 0 \tag{10}$$

where Ω is the control volume and $\boldsymbol{S}$ is the boundary surface. The vector $\boldsymbol{W}$ contains the conservative variables:

$$\boldsymbol{W} = \{\rho, \rho u, \rho v, \rho w, \rho E\}^T \tag{11}$$

where ρ is the fluid density, u, v, and w are the three Cartesian velocity components and the flow specific total energy E is given by

$$E = e + \frac{u_i u_i}{2} \tag{12}$$

where e is the internal energy.

The flux tensors $\boldsymbol{f}$ and $\boldsymbol{f}_\mu$ in Eq. (10) represent the inviscid convective fluxes and the diffusive fluxes, respectively. The convective flux $\boldsymbol{f}$ defined in terms of the relative velocity $\boldsymbol{u} - \boldsymbol{u}_b$ is

$$f = \begin{bmatrix} \rho(u-u_b) & \rho(v-v_b) & \rho(w-w_b) \\ \rho u(u-u_b) + p & \rho u(v-v_b) & \rho u(w-w_b) \\ \rho v(u-u_b) & \rho v(v-v_b) + p & \rho v(w-w_b) \\ \rho w(u-u_b) & \rho w(v-v_b) & \rho w(w-w_b) + p \\ \rho\left(E+\frac{p}{\rho}\right)(u-u_b) & \rho\left(E\frac{p}{\rho}\right)(v-v_b) & \rho\left(E+\frac{p}{\rho}\right)(w-w_b) \end{bmatrix} \tag{13}$$

where $\boldsymbol{u}_b = (u_b, v_b, w_b)^T$ is the grid velocity vector. The diffusive fluxes due to the viscous shear stresses, thermal diffusion, and turbulence diffusion can be written as

where $\tau_{\alpha\beta}$ with $\alpha, \beta \in \{x, y, z\}$ is the stress tensor expressed as

$$\tau_{\alpha\beta} = \mu(\partial_\alpha u_\beta + \partial_\beta u_\alpha) - \frac{2}{3}\mu\delta_{\alpha\beta}\partial_\alpha u_\beta \tag{15}$$

and

$$q_\alpha = -k\partial_\alpha \Theta \tag{16}$$

In the preceding equations, μ represents the dynamic viscosity, k is the thermal conductivity, and Θ is the temperature. The stress tensor $\tau_{\alpha\beta}$ is the general form of the shear stresses in $\boldsymbol{f}_\mu$.

The fluid governing equations can be discretized into the following semidiscrete form:

$$\frac{\mathrm{d}w}{\mathrm{d}t} + R(w) = 0 \tag{17}$$

By applying the dual-time method with a second-order implicit scheme, Eq. (17) could be reformulated into the following forms:

$$\frac{\mathrm{d}w^{n+1}}{\mathrm{d}t^*} + R^*(w^{n+1}) = 0 \tag{18}$$

and

$$R^*(w^{n+1}) = \frac{3w^{n+1} - 4w^n + w^{n-1}}{2\Delta t} + R(w^{n+1}) \tag{19}$$

The spatial discretization in the preceding equations is done based on a finite volume approach. The cell-centered-based method is used to calculate gradients. The discretization of the convective fluxes is based on a second-order Roe's flux-difference splitting scheme for Navier–Stokes equations. The discretization of the diffusive fluxes is based on a second-order artificial or matrix dissipation scheme. To cope with the complicated moving mesh cases, a structured multiblock mesh is generated [20].

2. Structural Dynamics

The structural elastic equations could be discretized in a finite element model as follows:

$$M\ddot{x}_s + C\dot{x}_s + Kx_s = F \tag{20}$$

where M denotes the mass matrix, C represents the structural damping matrix, K is the stiffness matrix, and F is the fluid dynamic force acting on the object surface.

By finding the mode shape $\tilde{\boldsymbol{\Phi}}$, a relationship equation could be defined as

$$x_s = \tilde{\Phi} q \tag{21}$$

where $\boldsymbol{q}$ is the vector of the principal coordinates. Equation (20) can be premultiplied by the transpose mode shape $\tilde{\boldsymbol{\Phi}}^T$ as

$$\tilde{\Phi}^T M\tilde{\Phi}\,\ddot{q} + \tilde{\Phi}^T C\tilde{\Phi}\,\dot{q} + \tilde{\Phi}^T K\tilde{\Phi} q = \tilde{\Phi}^T F \tag{22}$$

By assuming linear combination between damping matrix and mass and stiffness matrices, Eqs. (21) and (22) could be decoupled and the jth equations are shown as

Table 1 Time-step sensitivity study for a oscillating rigid foil at $f^* = 0.18$ and $\theta_0 = 60$ deg

No. of time steps per cycle	Iterations within one time step	Time-averaged C_{op}
128	400	0.433
64	300	0.432
32	200	0.406

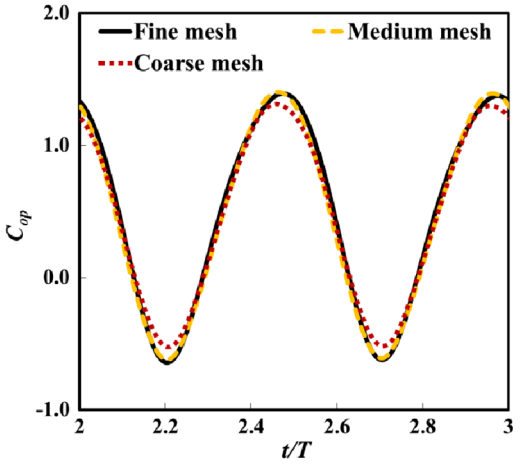

Fig. 4 Mesh number sensitivity study for an oscillating rigid foil at $f^* = 0.18$ and $\theta_0 = 60$ deg.

$$\ddot{q}_j + 2\zeta_j\omega_j\dot{q}_j + \omega_j^2 q_j = \frac{\tilde{\phi}_j}{m_j}F \tag{23}$$

and

$$\Delta x_s = \sum_{j=1}^{N} q_j\tilde{\phi}_j \tag{24}$$

where ζ_j is the modal damping ratio, ω_j is the natural frequency, and m_j is the mass matrix in the jth diagonal element. The jth element of mode shape $\tilde{\Phi}^T$, $\tilde{\phi}_j^T$ is defined as

$$\tilde{\Phi}^T = [\tilde{\phi}_1, \tilde{\phi}_2, \tilde{\phi}_3, \ldots, \tilde{\phi}_N]^T \tag{25}$$

Following Alonso and Jameson [29], the first-order differential equations are defined as

$$x_{1j} = q_j \tag{26}$$

$$\dot{x}_{1j} = x_{2j} \tag{27}$$

and

$$\dot{x}_{2j} = \frac{\tilde{\phi}_j^T}{m_j}F - 2\zeta_j\omega_j x_{2j} - \omega_j^2 x_{1j} \tag{28}$$

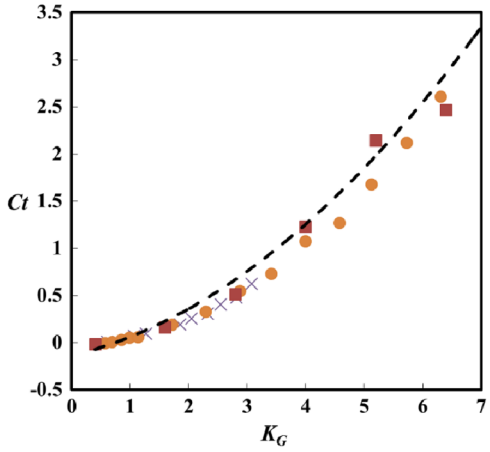

a) Thrust coefficient

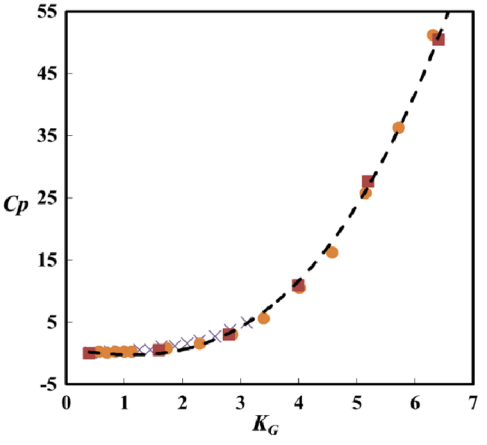

b) Power coefficient

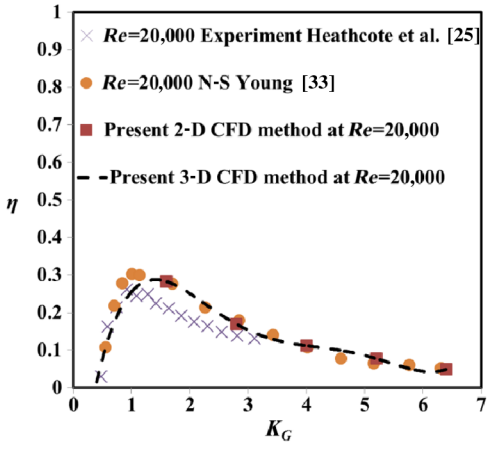

c) Efficiency

Fig. 5 Validation results of a 3-D rigid flapping foil with $\mathcal{R} = 3.0$.

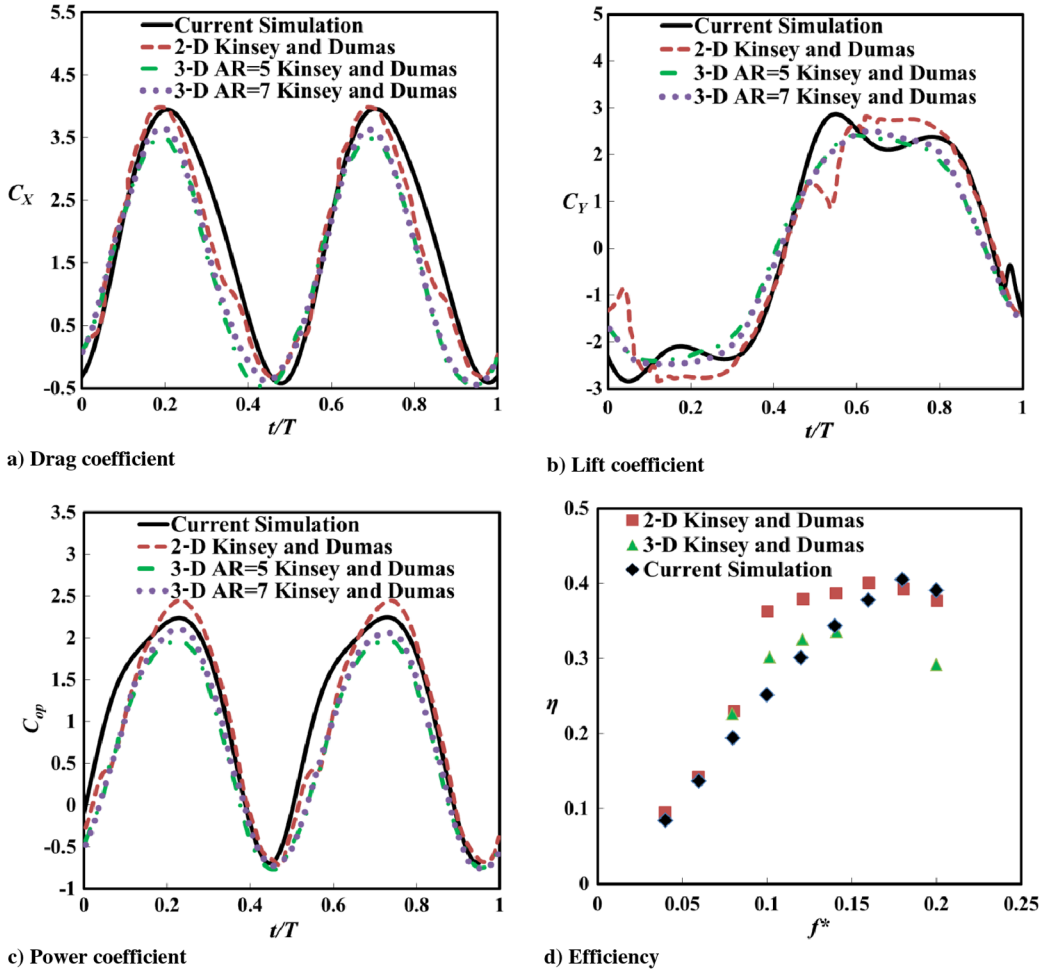

Fig. 6 Validation on a rigid oscillating foil as an energy extraction device with $Re = 5 \times 10^5$, $h_0/c = 1.0$, $c_{\text{pit}}/c = 1/3$; $\theta_0 = 75$ deg, and $\varphi = -\pi/2$; comparison with Kinsey and Dumas [5,9].

Thus, the model equation could be rewritten as

$$\dot{X}_j = A_j X_j + F_j, \qquad j = 1, \ldots, N \tag{29}$$

where

$$\dot{X}_j = \begin{bmatrix} \dot{x}_{1j} \\ \dot{x}_{2j} \end{bmatrix} \tag{30}$$

$$A_j = \begin{bmatrix} 0 & 1 \\ -\omega_j^2 & -2\zeta_j\omega_j \end{bmatrix} \tag{31}$$

and

$$F_j = \begin{bmatrix} 0 \\ \frac{\tilde{\phi}_j^T}{m_j} F \end{bmatrix} \tag{32}$$

Then, the model equation can be further discretized by the pseudotime t^* as

$$\frac{\mathrm{d}z_j^{n+1}}{\mathrm{d}t^*} + R_s^*(z_j^{n+1}) = 0 \tag{33}$$

and

$$R_s^*(z_j^{n+1}) = \frac{3z_j^{n+1} - 4z_j^n + z_j^{n-1}}{2\Delta t} + R_s(z_j^{n+1}) \tag{34}$$

where

$$z_j = \begin{bmatrix} z_{1j} \\ z_{2j} \end{bmatrix} \tag{35}$$

and

$$\frac{\mathrm{d}z_{(1,2)j}}{\mathrm{d}t^*} = \omega_j(-\zeta_j \pm \sqrt{\zeta_j^2 - 1})z_{(1,2)j} + \frac{\sqrt{\zeta_j^2 - 1} \mp \zeta_j}{2\sqrt{\zeta_j^2 - 1}} \frac{\tilde{\phi}_j^T}{m_j} F \tag{36}$$

In the current in-house code, Eq. (33) is coupled with Eq. (18). Specifically, the foil displacement data are employed by the fluid residual calculation as the flow boundary condition and the fluid parameters employed by the structure residual calculation as the hydrodynamic forcing. The detailed fluid–structure coupling algorithm is provided in the following.

3. *Fluid–Structure Coupling*

Because the fluid domain and the structure domain are calculated independently during the iterations, it is necessary to pass the fluid load from the fluid solver to the structure solver to calculate the structure deformation and pass the structure displacement from the structure solver to the fluid solver as the boundary conditions to calculate the fluid forces. A linear transformation equation between the fluid and structure domains is used to exchange information between them. The displacement Δx_f of the fluid dynamic grid is expressed in terms of the structural grid displacements Δx_s using a transformation matrix $\boldsymbol{S}$ as

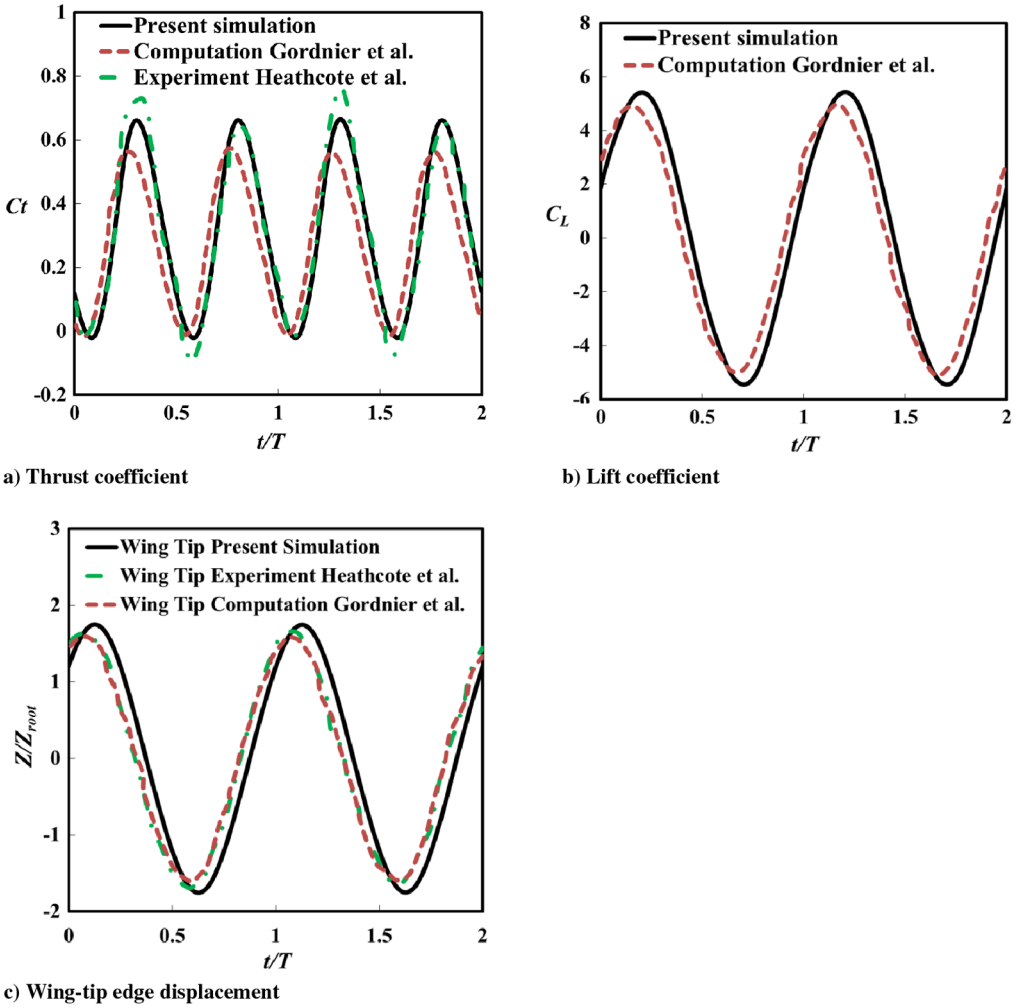

Fig. 7 Validation on a flexible 3-D plunging wing in water flow.

$$\Delta x_f = S\Delta x_s \tag{37}$$

Because the motion of every node needs to meet the requirements of conservation of work, both fluid mesh nodes and structure mesh nodes have to obey the following equations:

$$f_s^T \Delta x_s = f_f^T \Delta x_f \tag{38}$$

Equations (37) and (38) lead to

$$\Delta f_s = S^T \Delta f_f \tag{39}$$

In the preceding transformation equations, $\boldsymbol{f}_s$ represents the force vector acting on the structure nodes and $\boldsymbol{f}_f$ represents the force vector acting on the fluid nodes.

To find a proper transformation matrix $\boldsymbol{S}$, the constant-volume tetrahedron (CVT) method is used. Because the volume of each associated tetrahedron should be a nonzero value and kept as a constant during the structural deformation, the CVT method can only be adopted to three-dimensional fluid–structure interaction (FSI) modeling. Therefore, all two-dimensional cases in the present study are simulated by using a three-dimensional model. The details of this modeling strategy are described in the following.

4. Numerical Issues

The computational domain and mesh for both the fluid and the structure are shown in Fig. 3. The model size in the spanwise direction is one chord length. As suggested in the literature [30–32], applying the symmetry boundary condition (SBC) at the tips of the foil can effectively mitigate the three-dimensional (3-D) effects and achieve two-dimensional simulation. It is therefore used in the following two-dimensional simulations.

The structure nodes are applied as an inline mesh along the foil centerline, shown in the lower left corner of Fig. 3a. An example of the CVT association between the fluid node and structure nodes is displayed in the top right corner of Fig. 3a. A uniform constant velocity in the x direction is applied as the incoming flow for the far-field boundary condition for both inlet and outlet boundaries. The foil is set to be $50c$ (where c is the foil chord length) away from the incoming flow and outflow boundaries. The two-dimensional view for both fluid mesh and structure mesh are shown in Figs. 3b and 3c, respectively. The grid resolution test (as shown in Fig. 4) and time-step sensitivity study (as shown in Table 1) are carried out for the present study. A medium mesh at a time step of $\Delta t = T/64$ with 300 iterations per time step is selected in the following simulation to achieve a good calculation accuracy with an acceptable calculation time.

C. Validations

The numerical algorithms applied herein have been extensively validated in our previous publications (see [7,8,20]). In the current study, further investigations on a three-dimensional plunging-wing propeller have been conducted. The results predicted by our numerical model at $Re = 20{,}000$ are compared with the results by Heathcote et al. [25] and Young [33] in Fig. 5, where the nondimensional Garrick frequency K_G is defined as $K_G = \pi f_0 c/U_\infty$. Both three- and two-dimensional (whose mesh have the same topological structure as that in X-Y cross section of the three-dimensional model)

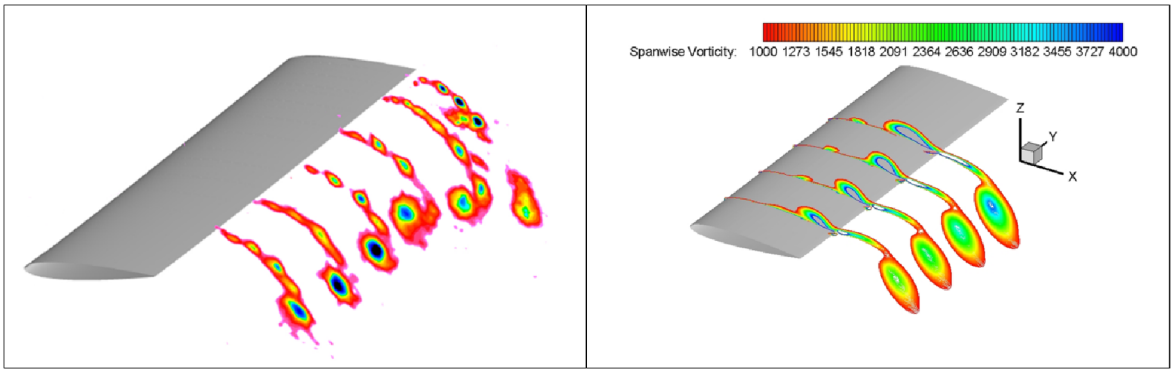

a) t/T=0.00 (Heathcote et al. [25] experimental result) b) t/T=0.00 (present numerical results)

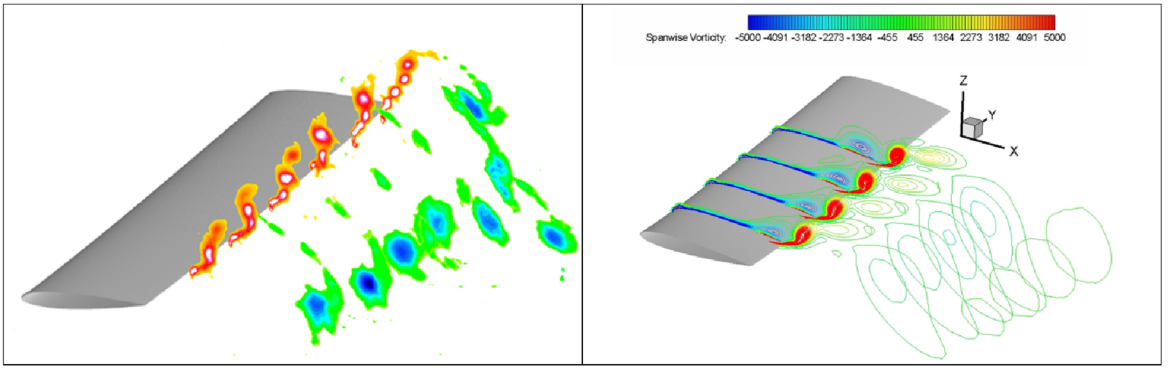

c) t/T=0.25 (Heathcote et al. [25] experimental result) d) t/T=0.25 (present numerical results)

Fig. 8 Validation results on spanwise vorticity contour for a flexible 3-D wing.

simulations, using our in-house code, have been compared with these results. Good agreement is shown in all cases.

To test the accuracy of our model in predicting flow energy harvesting, we examine the dynamics and energy harvesting performance of a pitching and heaving wing with $Re = 5 \times 10^5$. In that case, the plunging amplitude is the same as the chord length. The foil pitches at one-third chord length from its leading edge and pitch amplitude is 75 deg. The phase angle between heave and pitch is $\pi/2$. The time histories of drag, lift, and power coefficients at a reduced frequency of 0.14 are shown in Fig. 6a–6c, and the dependence of the time-averaged energy extraction efficiency upon the reduced frequency is shown in Fig. 6d. In general, our predicted data compare well with the published results of Kinsey and Dumas [5,9]. Some discrepancies are found between our results and theirs at large flapping frequency. We believe that this could be attributed to the different flow solvers and turbulence models being used by the authors. In the work of Kinsey and Dumas [5,9], a commercial computational fluid dynamics (CFD) solver FLUENT, with the one-equation Spalart–Allmaras turbulence model, was used. In our present study, an in-house code with a two-equation k-ω model is adopted.

To validate the capability of this code in solving fluid–structure coupling problems, additional simulation is performed for a three-dimensional flapping wing with spanwise flexibility and compared with the experimental results by Heathcote et al. [25] and numerical results by Gordnier et al. [26,28]. Two different types of flexible material (i.e., effective stiffness of 2.14×102 and 4.07×101) are studied and the instantaneous plots of some predicted parameters and flowfields are compared with Heathcote et al. [25] and Gordnier et al. [26]. The problem addressed is a three-dimensional NACA 0012 rectangular wing with a heaving motion in water at $Re = 3 \times 10^4$. The chord length is 0.1 m and the span length is 0.3 m. The plunging amplitude is 1.75×10^{-2} m with the oscillating frequency of 1.74 Hz. To construct the chordwise flexibility, a thin stiffener along the centerline of the foil is used, which is covered with a PDMS rubber. The thickness of the stiffener is 10^{-2} chord length. In the foil with effective stiffness of 2.14×10^2, the material properties of the stiffener are chosen so that Young's modulus is of 210 GPa and 7.8 density ratio. The instantaneous thrust, foil tip displacement, and lift coefficient are shown in Figs. 7a–7c. The vorticity contours at two instantaneous time of $t/T = 0$ and 0.25 are compared in Fig. 8 with the experimental results. In the wing with effective stiffness of 4.07×10^1, Young's modulus is set as 70 GPa and the density ratio as 2.7 [28]. Corresponding results are presented in Fig. 9. It is observed that the instantaneous lift and drag coefficients and vorticity contours compare fairly well with the results of Heathcote et al. [25] and Gordnier et al. [26]. All of the preceding results prove the accuracy of our code to cope with fluid–structure interaction problems.

III. Results

We start our investigation by using real metal materials for the stiffener. Specifically, two types of material are used, copper (Cu) and tungsten carbide (WC). This is because copper is a common metal with relatively high flexibility. Tungsten carbide, on the other hand, possesses a large Young's modulus coefficient and density. The detailed parameters used in our study are listed in Table 2. Numerical simulations are carried out for the preceding two stiffener materials and the results are compared with those with a rigid foil. Two pitching amplitudes, 60 and 75 deg, are applied. These are close to the pitching amplitudes with high-efficiency energy harvesting (see, e.g., [4]). The effective stiffness is 5.25×10^1 and 2.62×10^2 for copper and tungsten carbide stiffeners, respectively.

A. Energy Harvesting Performance with Stiffeners of Real Materials

As shown in Eq. (5), the key parameter to quantify the energy extraction performance of an oscillating foil device is the efficiency η. In Fig. 10a, we compare the energy extraction efficiency of the copper stiffener foil (hereafter referred to as Cu), the tungsten carbide stiffener foil (referred to as WC), and the rigid foil at different reduced frequencies. Based on these results, flexible foils show a certain level of improved performance as compared with their rigid counterparts.

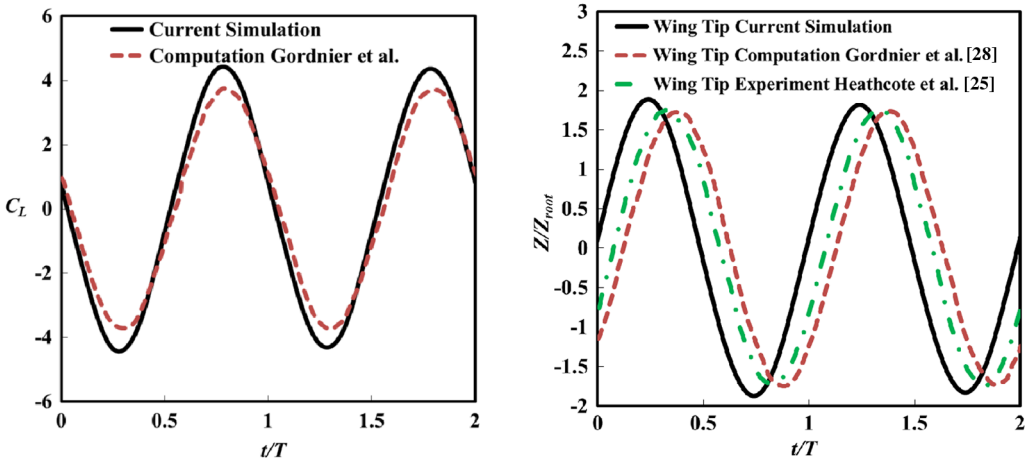

a) Lift coefficient b) Wing-tip edge displacement

Fig. 9 Validation results on a very flexible 3-D plunging wing ($Re = 3.0 \times 10^4$) $AR = 3.0$, $h_0 = 1.75 \times 10^{-2}$ m, $f_0 = 1.74$ Hz, $\Pi = 4.07 \times 10^1$, $E = 70$ GPa, and DR = 2.7; comparison with Heathcote et al. [25] and Gordnier et al. [28].

For example, the peak efficiency of WC reaches 20% at the pitching angle of 60 deg and 43% at the pitching angle of 75 deg, whereas the corresponding results for the rigid foil are 19 and 35%, respectively. Cu also reaches 36% at 60 deg pitching angle. The efficiency enhancement of Cu (compared with the rigid foil) is 17.4% at a reduced frequency of 0.15 and 32.2% with $f^* = 0.25$. Because the structural model used herein is linear, which is not accurate in simulating large deformations, it is not used to study cases with low stiffness at high pitching angle.

Within the large reduced frequency region ($f^* = 0.18 - 0.25$), where rigid foils usually present a decayed performance or even degrade to negative power extraction, both Cu and WC flexible foils still exhibit a positive energy extraction with the efficiency much higher than that of the rigid foil.

The trailing-edge displacement amplitude β_{0_amp} shows different magnitudes and variation trends for the two flexible foils, as displayed in Fig. 10b. Because of the small Young's modulus coefficient for Cu, the trailing-edge displacement of Cu is larger than that of WC. For Cu, the maximum value of such displacement is around 0.063. Apart from the time-averaged results, the instantaneous displacement and force results at a reduced frequency of 0.18 are picked up for a detailed analysis.

The instantaneous trailing-edge displacement for the two flexible foils and the rigid foil are plotted in Fig. 11a. It is clear that the peak value of 0.055 is reached at $t/T = 3/8$ for the Cu foil. Large trailing-edge displacement is achieved during $t/T = 2/8$ and $3/8$ for the WC foil.

Figure 11b shows the lift coefficient along with the foil heaving velocity (dh/dt). It is observed that the structural flexibility significantly increases the peak lift coefficient (as shown in the curve of Cu). In addition, within the time frame from $t/T = 2/8$ to $4/8$, the flexible foils achieve higher C_L than the rigid foil. As concluded by Xiao et al. [8], it has a positive contribution to the time-mean efficiency over one cycle if the force or moment has the same sign as the heaving or pitching velocity. Therefore, an increased C_L in the aforementioned time frames contributes positively to the overall efficiency.

The variations of moment coefficient M_Z and the pitch velocity ($d\theta/dt$) are presented in Fig. 11c. A phase lag of 180 deg for M_Z and $d\theta/dt$ is shown so that the pitching motion contributes negatively to the overall energy extraction. The flexibility of the foil leads to a slight decrease in M_Z during $t/T = 0/8$ and $3/8$, reducing the power

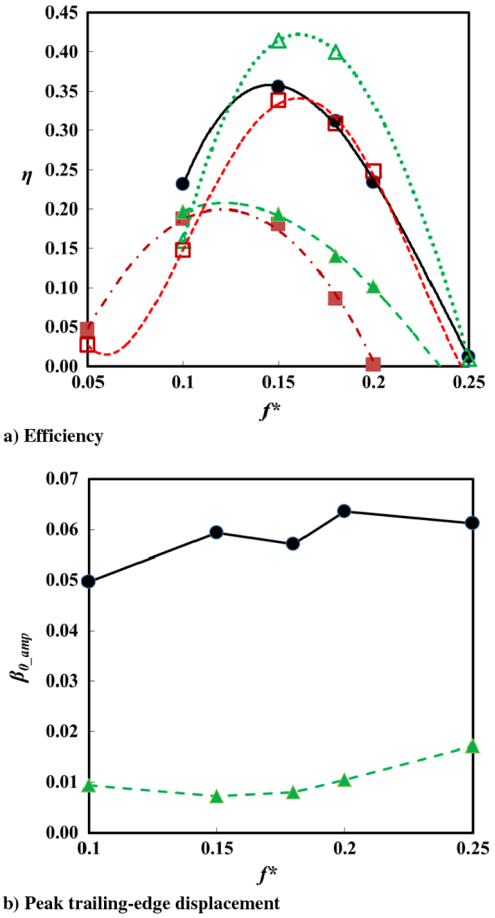

a) Efficiency

b) Peak trailing-edge displacement

Fig. 10 Overall performance of a flexible oscillating foil device with $h_0/c = 1.0$. ●: Cu = 60 deg; ▲: WC = 60 deg; ■: Rigid = 60 deg; □: Rigid = 75 deg; △: WC = 75 deg.

expenditure in pitching so that the overall energy harvesting performance is improved. The instantaneous power coefficient is shown in Fig. 11d. It is clear that, with flexible foils, the positive

Table 2 Case summary for real materials

Case	Material	Young's modulus coefficient	DR	Effective stiffness Π	Poisson ratio	Natural frequency ratio
1	Copper	1.12×10^8	8.9	5.25×10^1	0.34	7.55
2	Tungsten carbide	5.61×10^8	15.6	2.46×10^2	0.24	12.76

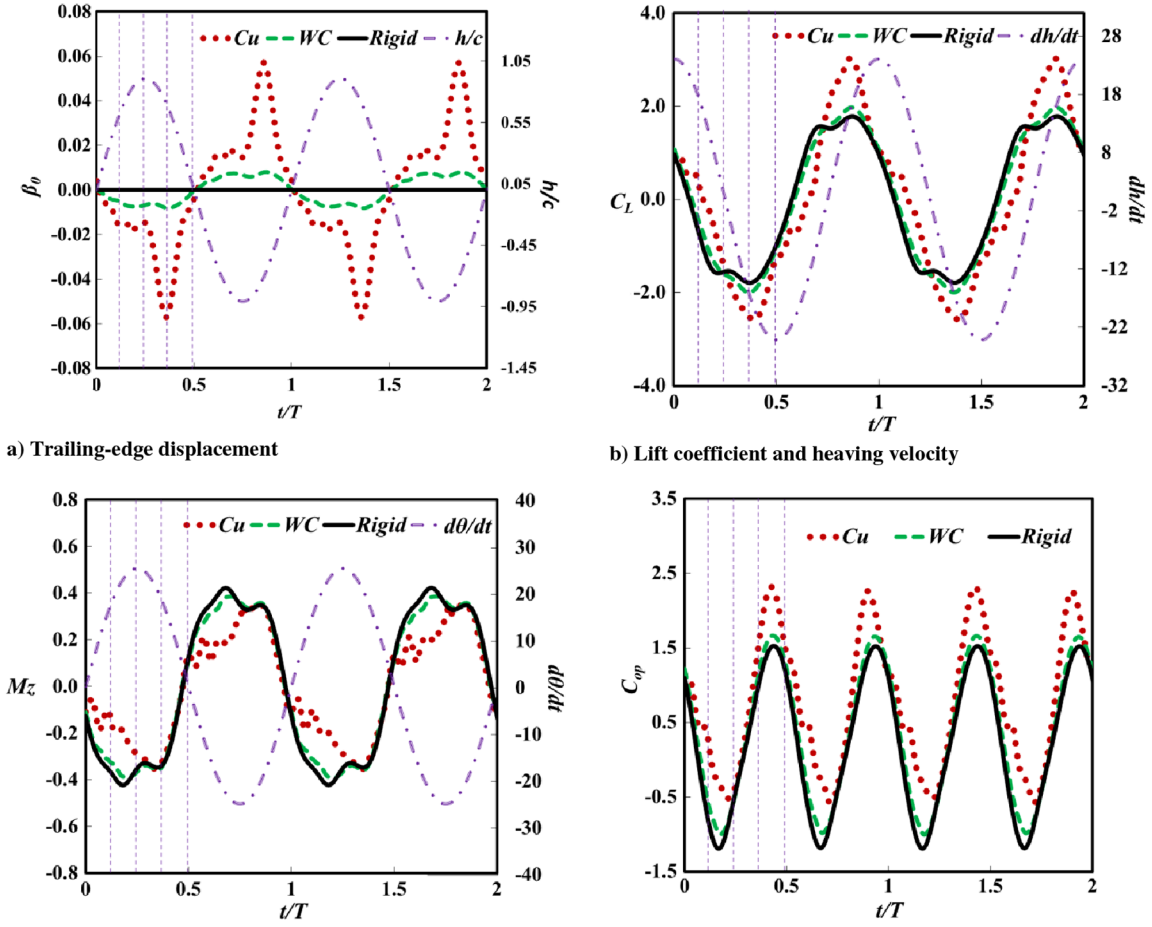

Fig. 11 Time histories for foils with Cu and WC stiffeners at $f^* = 0.18$ and $\theta_0 = 60$ deg.

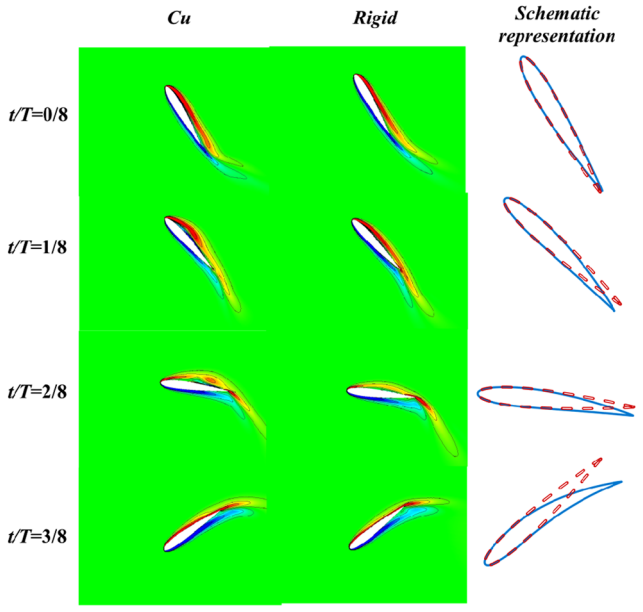

Fig. 12 Vorticity contours and schematic representation of foil kinematics.

instantaneous power is enhanced, whereas the negative power is reduced.

Figure 12 shows the vorticity contour for Cu, WC, and the rigid foil at $f^* = 0.18$ and pitch amplitude of 60 deg within half an oscillating period. In the schematic plot, the flexible foil is shown with solid lines with a five times scale of original displacement, and the rigid foil is

Table 3 Case summary for virtual materials used to test Young's modulus effect[a]

Case	Young's modulus coefficient	Effective stiffness Π	Natural frequency ratio
1	8.15×10^7	3.82×101^1	6.44
2	1.12×10^8	5.25×101^1	7.55
3	2.55×10^8	1.19×10^2	11.38
4	5.61×10^8	2.62×10^2	16.88
5	7.65×10^8	3.58×10^2	19.71
6	1.02×10^9	4.77×10^2	22.75

[a]Poisson ratio ν for all cases is 0.34.

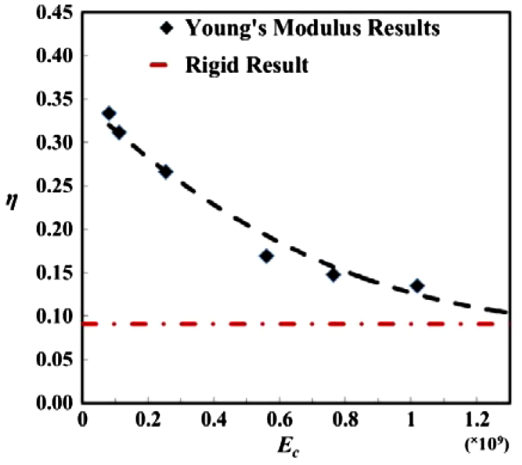

Fig. 13 Young's modulus coefficient effect on the efficiency of a flexible foil at $f^* = 0.18$ and $\theta_0 = 60$ deg.

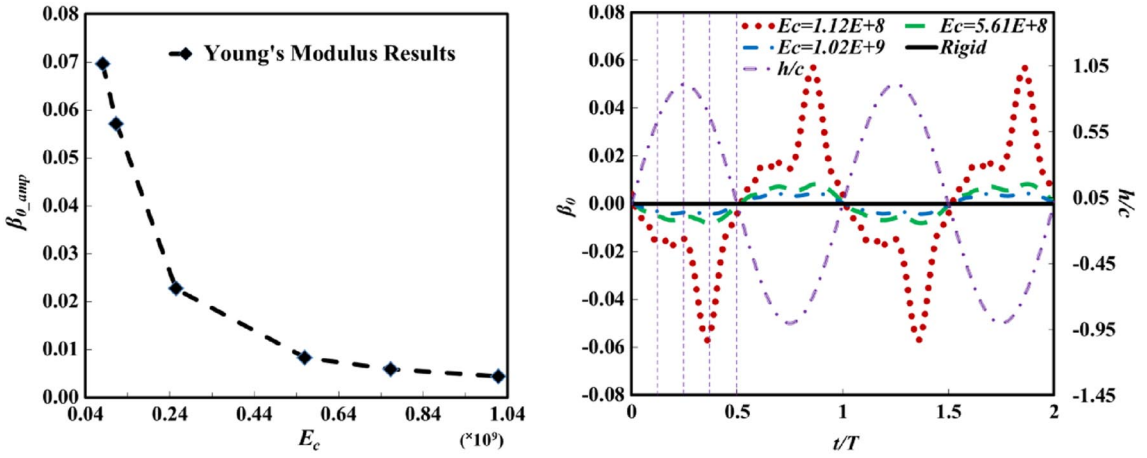

a) Trailing-edge displacement amplitude vs Young's modulus

b) Instantaneous trailing-edge displacement

Fig. 14 Trailing-edge deformations of a flexible foil with different Young's modulus coefficient at $f^* = 0.18$ and $\theta_0 = 60$ deg.

shown as dashed lines. The most pronounced characteristic of the flexible foils compared with the rigid foil is the enhanced leading-edge vortices. This is explained by the synchronization between the development of LEVs and the foil deformation. As demonstrated in Fig. 12, at $t/T = 0$, the centerline of the foil is almost straight and the vorticity generated from the leading edge is attached to the upper surface of the foil. At $t/T = 1/8$, the hinder part of the foil starts bending downward, making it hard for the leading-edge vorticity to remain attached. This encourages the separation of the leading-edge vorticity and the growth of the leading-edge vortex. As indicated in past papers [34–36], the strength of leading-edge vortices is closely associated with the energy harvesting performance. Enhanced leading-edge flow separation and well-formed leading-edge vortices usually lead to high efficiency (see [34], figures 7 and 8). With available results presented in this section, the flexible effect has little influence on the timing of LEVs. As seen from Figs. 11b and 11c, the difference in phase between a flexible blade and a rigid blade for its lift and moment coefficients is not as pronounced as the difference in

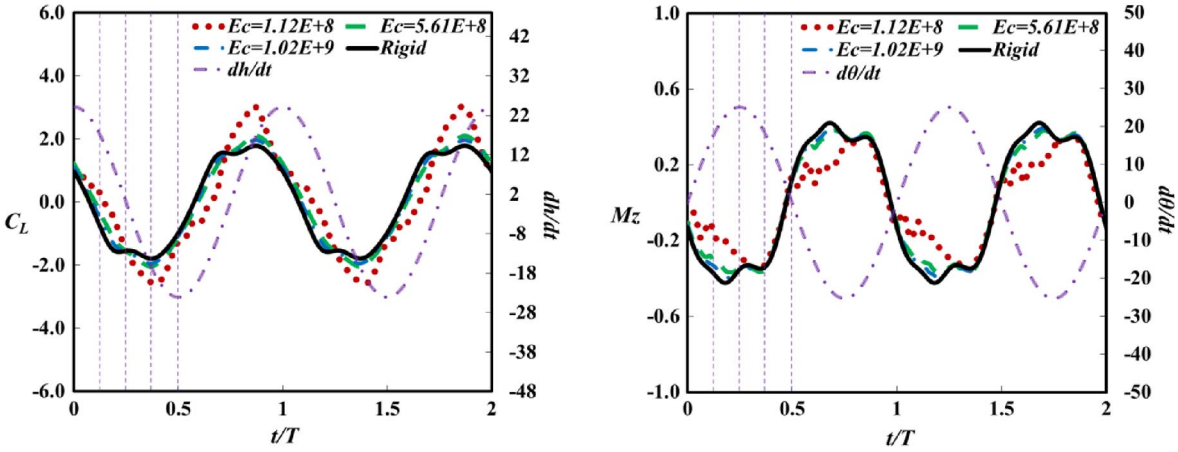

a) Lift coefficient and heaving velocity pitching velocity

b) Moment coefficient and pitching velocity

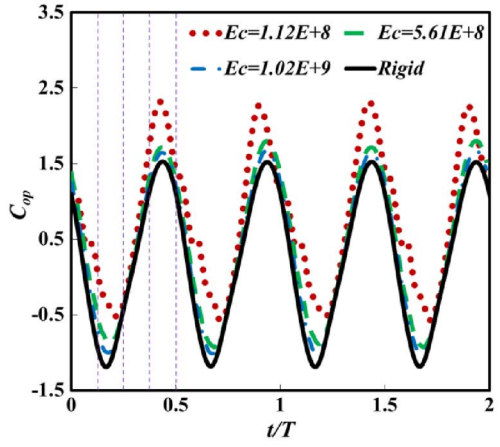

c) Power coefficient

Fig. 15 Time histories for Young's modulus coefficient effect at $f^* = 0.18$ and $\theta_0 = 60$ deg.

Table 4 Case summary for virtual materials used to test density ratio effect[a]

Case	DR	Natural frequency ratio
1	7.0	8.54
2	8.9	7.55
3	12.0	6.53
4	15.6	5.72
5	20.0	5.05
6	30.0	4.13
7	70.0	2.70
8	700.0	0.85
9	1000.0	0.72
10	1200.0	0.65
11	1500.0	0.58

[a]Effective stiffness Π and Poisson ratio ν for all cases are 5.25×10^1 and 0.34, respectively.

amplitude. This can also be confirmed by the contour plots in Fig. 12. It seems that the flexibility enlarges the leading-edge flow separation region and thus increases the LEV strength, leading to an increase of optimal f^*.

When studying the flexible wing or membrane problems, previous researchers [25–27] often used real materials with specific combinations of material properties (e.g., Young's modulus and density) as we did herein. On the other hand, several studies [14,27] suggest that it is more interesting to decouple Young's modulus and the density ratio and examine their effects independently. Hereby, we will study the effects of these two parameters separately by constructing some virtual materials with 1) a constant density ratio but variable Young's modulus and 2) constant Young's modulus with different density ratios. In these cases, the foil oscillation reduced frequency is fixed as 0.18 and the pitching amplitude is set as 60 deg.

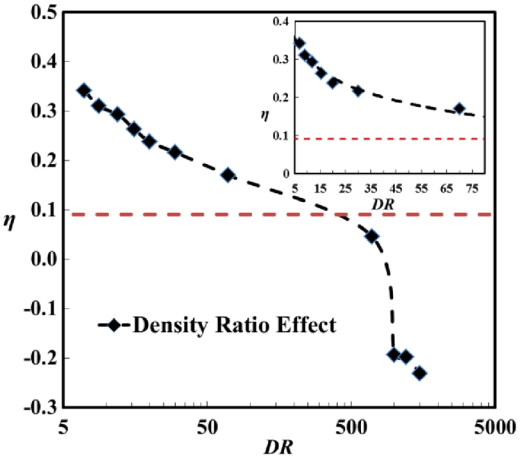

Fig. 16 Density ratio effect on the efficiency of a flexible foil at $f^* = 0.18$ and $\theta_0 = 60$ deg.

B. Young's Modulus Effect

In this part, six different Young's modulus coefficients ranging from 8.15×10^7 to 1.02×10^9 are investigated (further reduction of Young's modulus coefficient leads to large foil deformations that are

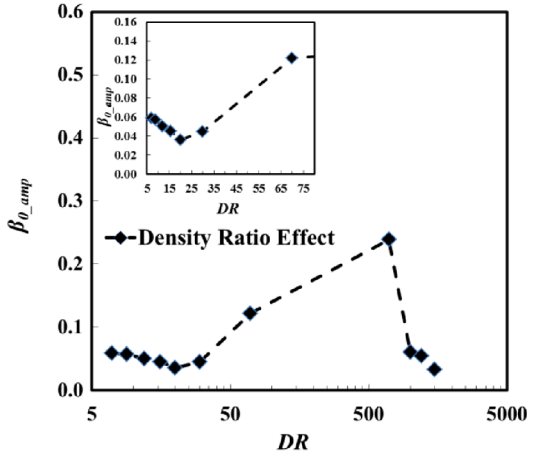

a) Trailing-edge displacement amplitude vs density ratio

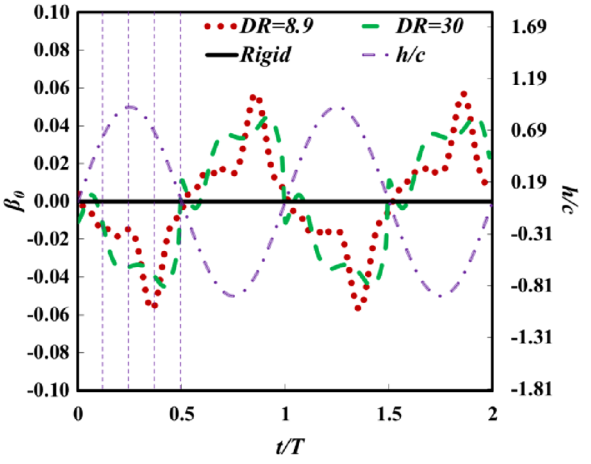

b) Instantaneous trailing-edge displacement (DR=8.9 and 30, rigid foil)

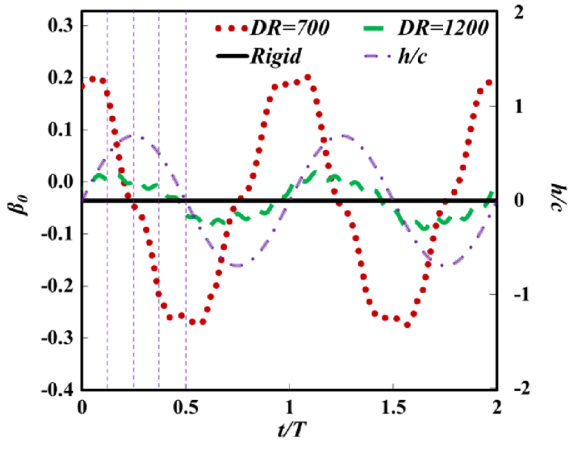

c) Instantaneous trailing-edge displacement (DR=700, 1200, and rigid foil)

Fig. 17 Density ratio effect at $f^* = 0.18$ and $\theta_0 = 60$ deg.

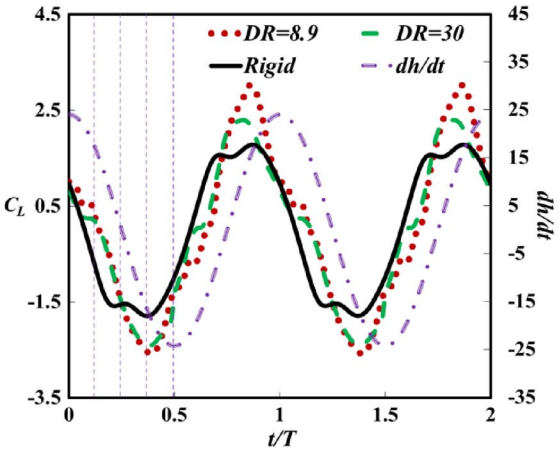

a) Lift coefficient and heaving velocity

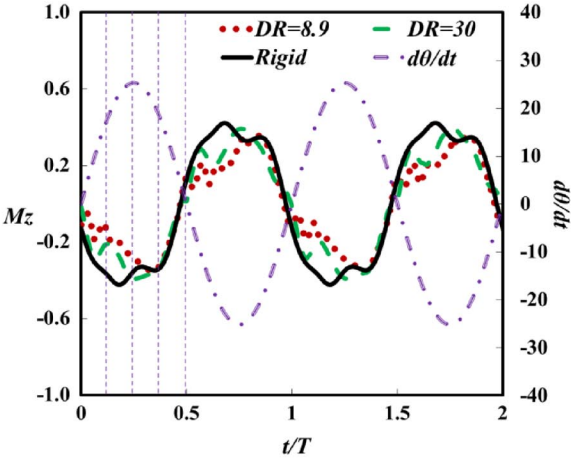

b) Moment coefficient and pitching velocity

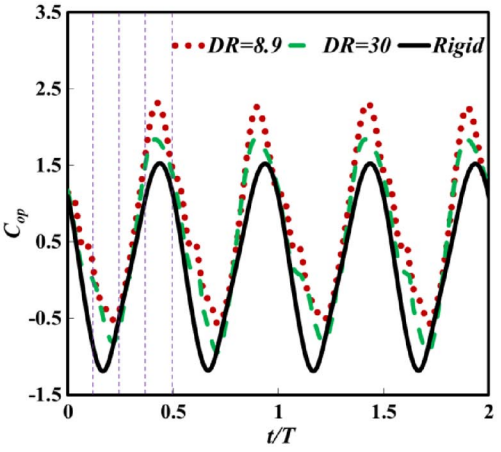

c) Power coefficient

Fig. 18 Time histories with low-density ratios (DR = 8.9 and 30) at $f^* = 0.18$ and $\theta_0 = 60$ deg.

beyond the capacity of the linear structural model). The density ratio is set as 8.9. The effective stiffness for these cases varies from 3.82×101^1 to 4.77×102^2, accordingly. The detailed parameters are summarized in Table 3.

Figure 13 shows the variation of the energy extraction efficiency with Young's modulus coefficient. With the increase of Young's modulus, the efficiency decreases and eventually approaches the rigid foil result. An empirical formulation is generated to quantify this curve and expressed as:

$$\eta = a_1 {E_c}^2 + a_2 {E_c}^2 + a_3 E_c + a_4, \quad (8.15 \times 10^7 \le E_c \le 1.01 \times 10^9) \tag{40}$$

where $a_1 = 2 \times 10^{-29}$, $a_2 = -2 \times 10^{-19}$, $a_3 = 4 \times 10^{-10}$, and $a_4 = 0.3487$.

The peak trailing-edge displacement at different values of Young's modulus coefficient is shown in Fig. 14a. Similar to the efficiency plot in Fig. 13, the displacement reduces rapidly with the increase of Young's modulus coefficient. This is well reflected by the profoundly smaller β_0 with larger E_c in Fig. 14b, where the instantaneous trailing displacement is shown within two oscillating periods.

The instantaneous lift coefficient C_L, moment coefficient M_Z, and power coefficients C_{op} are analyzed in Fig. 15. With the increase of Young's modulus coefficient, a drop of lift coefficient and moment coefficient can be seen in Figs. 15a and 15b. This leads to the drop of the instantaneous power (Fig. 15c). It agrees well with the tendency of the time-mean energy efficiency, as seen in Fig. 13.

C. Density Ratio Effect

In this part, nine density ratios ranging from 7 to 1500 are investigated with a fixed Young's modulus coefficient of 1.12×108^8. The detailed parameters are listed in Table 4.

Figure 16 shows the energy harvesting efficiency at various density ratios in a logarithmic graph. With the increase of the density ratio, the efficiency is dramatically decreased. As the density ratio becomes larger than 700, the foil switches from an energy extraction state (positive η) to an energy consumption state (negative η).

The variation of trailing-edge displacement with density ratio is shown in Fig. 17a. The maximum displacement occurs at DR = 700 with the magnitude of 0.239, which is actually quite large compared with the pitching angle of 60 deg.

In Figs. 17b and 17c, the instantaneous trailing-edge displacement with small density ratios (DR = 8.9 and 30) and large DRs (DR = 700, 1200, and rigid) are presented. Apart from the trend of peak β_0 variation with DRs, which is already shown in Fig. 17a, it is also noted that, when the density ratio is near 700, the instantaneous displacement profile presents a very regular sinusoid containing one dominant frequency. It is determined from our results that the phase difference between trailing-edge displacement and corresponding heave for small density ratios (DR < 700) is around 180 deg. However, when the density ratio is increased to 700, the phase lag becomes 90 deg. For DR = 1200, this angle changes to 0 deg. This phase variation is consistent with the response of an oscillator around its natural frequency.

When the DR is small, the foil deformation is mostly driven by the fluid forcing. For large values of DR, on the other hand, the effect of the inertia of the foil itself (herein, the inertia of the stiffener) becomes pronounced. To study the relative importance of these two effects, we

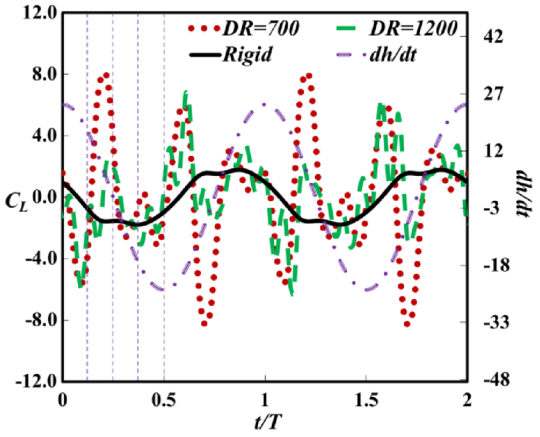

a) Lift coefficient and heaving velocity

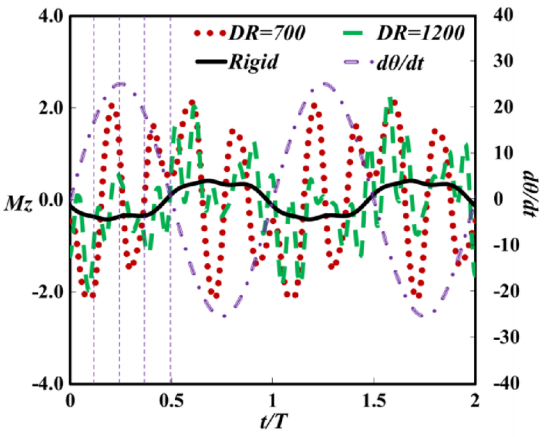

b) Moment coefficient and pitching velocity

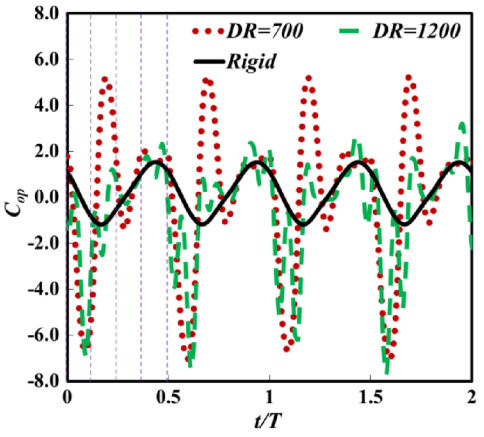

c) Instantaneous power coefficient

Fig. 19 Time histories with large density ratios (DR = 700 and 1200) at $f^* = 0.18$ and $\theta_0 = 60$ deg.

consider the ratio between mass of the stiffener and the added mass (which is a significant part of fluid forcing). In the heaving mode, this ratio is estimated as

$$\frac{\rho_s c_{\mathrm{sf}} T_{\mathrm{sf}}}{\pi \rho_f (c/2)^2} = 8.6 \times 10^{-3}\mathrm{DR} \tag{41}$$

According to this parameter, the effect of the foil inertia surpasses the fluid forcing effect when the density ratio is higher than 116.

Figures 18a–18c show the density ratio effect on the instantaneous lift, moment, and power coefficients associated with low-density ratios (DR = 8.9 and 30). It is clear that the difference of various density ratios mostly affects the peak lift coefficient, particularly within the time frames from $t/T = 2/8$ to $7/16$. In Figs. 19a–19c, the instantaneous plots are shown at large density ratios (DR = 700 and 1200). A large fluctuation occurs at DR = 700, which is under a resonance condition.

From the vorticity plots in Fig. 20, it is seen that cases with smaller density ratios are characterized by enhanced development of LEVs. An increased LEV generation, according to our discussion in Sec. III.A, is beneficial to energy extraction. Moreover, within the time slot between $t/T = 2/8$ and $3/8$, the LEV reattaches to the upper surface of the foil near the trailing edge, creating a counterclockwise moment. It coincides with the pitching motion of the foil at that instant so that it provides additional contribution to the energy harvesting. This beneficial effect is not achieved in cases with higher density ratio. In contrast, for these cases (e.g., DR = 700 or 1200), during the counterclockwise pitching motion of the foil, there is significant vorticity attached to the lower surface of the foil near the trailing edge. The associated low pressure induces a clockwise moment so that there is negative contribution to energy harvesting.

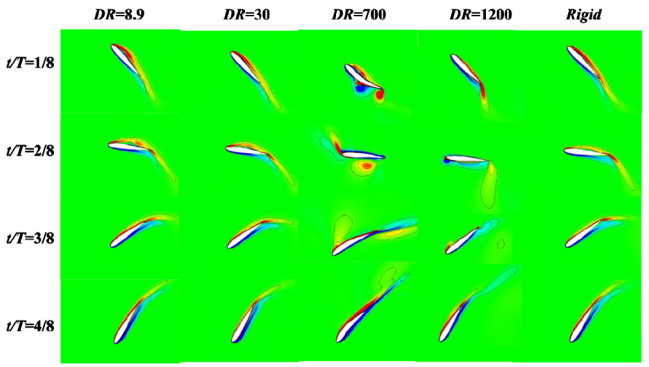

Fig. 20 Vorticity contours for density ratio effect at $f^* = 0.18$ and $\theta_0 = 60$ deg in half an oscillating period.

IV. Conclusions

Using a fully coupled fluid–structure interaction algorithm, the effect of structural flexibility upon the energy extraction capacity of an oscillating foil with realistic internal structure, characterized by a stiffener near the trailing edge, was numerically investigated. The power generation predicted by the model in this study is the net energy flux from the flowfield to the foil. In a real system (such as the one proposed by Kinsey and Dumas [5,6]), it is the extracted power minus the power input. For the stiffener, two types of real material (i.e., copper and tungsten carbide) are tested with their different effective stiffness and density ratios. To distinguish the effects of Young's modulus coefficient and density ratio to the dynamic response and energy extraction efficiency, cases were also studied

with the stiffener made of virtual materials with arbitrary Young's modulus and density.

The simulation shows that the passive structural flexibility in the vicinity of the trailing edge is capable of enhancing the overall energy extraction performance. Up to 32.2% increase in the efficiency is achieved by using a foil with copper stiffener. This is attributed to the enhancement of leading-edge vortices associated with the synchronization between vorticity generation/shedding and foil deformation. Within the range of parameters considered, both Young's modulus and density ratio affect the amplitude, as well as the phase lag between the deformation (characterized by the instantaneous trailing-edge displacement) and heave displacements. At sufficiently large density ratios, such change causes the oscillating foil to switch from energy extraction into energy consumption. A resonance phenomenon is also observed when the natural frequency of the foil coincides with its heaving frequency.

The beneficial effect of structural flexibility in the energy extraction of a flapping foil is reminiscent of the similar performance enhancement of flapping foil propellers using deformable structures (see, for example, [34–36]). There are, however, fundamental differences between these two phenomena. According to Katz and Weihs [35], the key mechanism of the propulsion efficiency increase in a chordwise flexible foil is that the overall fluid dynamic force is redirected more toward the front (see [35], figure 6). Another mechanism is that, in flexible propellers, the leading-edge separation is suppressed due to the reduction in the effective angle of attack at the leading edge. In contrast, the current research indicates that structural flexibility in an energy harvester actually encourages the development of leading-edge vortices (LEVs), leading to higher capacity in energy extraction.

A leading-edge flexibility study, where a flexible internal structure is installed in the leading-edge area, has also been performed. This structural design, however, leads to reduced efficiency according to the results (this is similar to the conclusion by Tian et al. [21], in which it is suggested that passive deformability at the leading edge is not beneficial to energy harvesting). Specifically, the passively induced instantaneous leading-edge deformation is 90 deg ahead of the foil heave displacement in phase. This leads to the decrease of the effective angle of attack at the leading edge and thus weakens the strength of LEVs.

Finally, in the present study, the flexible foil is modeled in two dimensions and thus only the bending motion is considered. In reality, a three-dimensional flexible wing may present a combined bending and twist motion under the external forces. Therefore, performing a fully three-dimensional fluid–structure interaction analysis to account for foil passive torsion and bending will be the next task in the near future. In addition, a more realistic device including an electromechanical transducer, which in general requires a semipassive or a fully passive device, will be investigated in future studies.

Acknowledgments

Results were obtained using the Engineering and Physical Sciences Research Council (EPSRC) funded ARCHIE-WeSt high-performance computer (www.archie-west.ac.uk) with EPSRC grant EP/K000586/1.

References

[1] Xiao, Q., and Zhu, Q., "A Review on Flow Energy Harvesters Based on Flapping Foils," *Journal of Fluids and Structures*, Vol. 54, No. 1, 2014, pp. 174–191. doi:10.1016/j.jfluidstructs.2014.01.002

[2] McKinney, W., and DeLaurier, J., "Wingmill: An Oscillating-Wing Windmill," *Journal of Energy*, Vol. 5, No. 2, 1981, pp. 109–115. doi:10.2514/3.62510

[3] Young, J., Lai, J., and Platzer, M. F., "A Review of Progress and Challenges in Flapping Foil Power Generation," *Progress in Aerospace Sciences*, Vol. 67, No. 3, 2014, pp. 2–28. doi:10.1016/j.paerosci.2013.11.001

[4] Kinsey, T., and Dumas, G., "Parametric Study of an Oscillating Airfoil in a Power-Extraction Regime," *AIAA Journal*, Vol. 54, No. 6, 2008, pp. 1318–1330. doi:10.2514/1.26253

[5] Kinsey, T., and Dumas, G., "Computational Fluid Dynamics Analysis of a Hydrokinetic Turbine Based on Oscillating Hydrofoils," *Journal of Fluids Engineering*, Vol. 134, No. 2, 2012, Paper 021104. doi:10.1115/1.4005841

[6] Kinsey, T., and Dumas, G., "Optimal Tandem Configuration for Oscillating-Foils Hydrokinetic Turbine," *Journal of Fluids Engineering*, Vol. 134, No. 3, 2012, Paper 031103. doi:10.1115/1.4005423

[7] Xiao, Q., and Liao, W., "Numerical Investigation of Angle of Attack Profile on Propulsion Performance of an Oscillating Foil," *Computers and Fluids*, Vol. 39, No. 8, 2010, pp. 1366–1380. doi:10.1016/j.compfluid.2010.04.006

[8] Xiao, Q., Liao, W., Yang, S., and Peng, Y., "How Motion Trajectory Affects Energy Extraction Performance of a Biomimic Energy Generator with an Oscillating Foil?" *Renewable Energy*, Vol. 37, No. 1, 2012, pp. 61–75. doi:10.1016/j.renene.2011.05.029

[9] Kinsey, T., and Dumas, G., "Three-Dimensional Effects on an Oscillating-Foil Hydrokinetic Turbine," *Journal of Fluids Engineering*, Vol. 134, No. 7, 2012, Paper 071105. doi:10.1115/1.4006914

[10] Michael, V., Altman, A., Eldredge, J. D., Garmann, D. J., and Lian, Y., "Résumé of the AIAA FDTC Low Reynolds Number Discussion Group's Canonical Cases," *48th AIAA Aerospace Sciences Meeting*, AIAA Paper 2010-1085, 2010.

[11] Nakata, T., and Liu, H., "Aerodynamic Performance of a Hovering Hawkmoth with Flexible Wings: A Computational Approach," *Proceedings of the Royal Society B: Biological Sciences*, Vol. 279, No. 1729, 2012, pp. 722–731. doi:10.1098/rspb.2011.1023

[12] Combes, S. A., and Daniel, T. L., "Flexural Stiffness in Insect Wings I. Scaling and the Influence of Wing Venation," *Journal of Experimental Biology*, Vol. 206, No. 17, 2003, pp. 2979–2987. doi:10.1242/jeb.00523

[13] Combes, S. A., and Daniel, T. L., "Flexural Stiffness in Insect Wings II. Spatial Distribution and Dynamic Wing Bending," *Journal of Experimental Biology*, Vol. 206, No. 17, 2003, pp. 2989–2997. doi:10.1242/jeb.00524

[14] Zhu, Q., "Numerical Simulation of a Flapping Foil with Chordwise or Spanwise Flexibility," *AIAA Journal*, Vol. 45, No. 10, 2007, pp. 2448–2457. doi:10.2514/1.28565

[15] Shoele, K., and Zhu, Q., "Leading Edge Strengthening and the Propulsion Performance of Flexible Ray Fins," *Journal of Fluid Mechanics*, Vol. 693, No. 16, 2012, pp. 402–432. doi:10.1017/jfm.2011.538

[16] Shoele, K., and Zhu, Q., "Performance of a Wing with Nonuniform Flexibility in Hovering Flight," *Physics of Fluids*, Vol. 25, No. 4, 2013, Paper 041901. doi:10.1063/1.4802193

[17] Shyy, W., Aono, H., Chimakurthi, S. K., Trizila, P., Kang, C. K., Cesnik, C. E., and Liu, H., "Recent Progress in Flapping Wing Aerodynamics and Aeroelasticity," *Progress in Aerospace Sciences*, Vol. 54, No. 7, 2010, pp. 284–327. doi:10.1016/j.paerosci.2010.01.001

[18] Daniel, T. L., and Combes, S. A., "Flexible Wings and Fins: Bending by Inertial or Fluid-Dynamic Forces?" *Integrative and Comparative Biology*, Vol. 42, No. 5, 2002, pp. 1044–1049. doi:10.1093/icb/42.5.1044

[19] Yin, B., and Luo, H., "Effect of Wing Inertia on Hovering Performance of Flexible Flapping Wings," *Physics of Fluids*, Vol. 22, No. 11, 2010, Paper 111902. doi:10.1063/1.3499739

[20] Liu, W., Xiao, Q., and Cheng, F., "A Bio-Inspired Study on Tidal Energy Extraction with Flexible Flapping Wings," *Bioinspiration and Biomimetics*, Vol. 8, No. 3, 2013, Paper 036011. doi:10.1088/1748-3182/8/3/036011

[21] Tian, F. B., Young, J., and Lai, J. C., "Improving Power-Extraction Efficiency of a Flapping Plate: From Passive Deformation to Active Control," *Journal of Fluids and Structures*, Vol. 51, No. 27, 2014, pp. 384–392. doi:10.1016/j.jfluidstructs.2014.07.013

[22] Jones, K. D., and Platzer, M. F., "Numerical Computation of Flapping-Wing Propulsion and Power Extraction," AIAA Paper 1997-0826, 1997.

[23] Jones, K. D., Lindsey, K., and Platzer, M. F., "An Investigation of the Fluid-Structure Interaction in an Oscillating-Wing Micro-Hydropower Generator," *Advances in Fluid Mechanics*, Vol. 36, No. 1, 2003, pp. 73–84.

[24] Heathcote, S., and Gursul, I., "Flexible Flapping Airfoil Propulsion at Low Reynolds Numbers," *AIAA Journal*, Vol. 45, No. 5, 2007, pp. 1066–1079.
doi:10.2514/1.25431

[25] Heathcote, S., Wang, Z., and Gursul, I., "Effect of Spanwise Flexibility on Flapping Wing Propulsion," *Journal of Fluids and Structures*, Vol. 24, No. 2, 2008, pp. 183–199.
doi:10.1016/j.jfluidstructs.2007.08.003

[26] Gordnier, R. E., Attar, P. J., Chimakurthi, S. K., and Cesnik, C. E., "Implicit LES Simulations of a Flexible Flapping Wing," AIAA Paper 2010-2960, 2010.

[27] Chimakurthi, S. K., Tang, J., Palacios, R., Cesnik, C. E., and Shyy, W., "Computational Aeroelasticity Framework for Analyzing Flapping Wing Micro Air Vehicles," *AIAA Journal*, Vol. 47, No. 8, 2009, pp. 1865–1878.
doi:10.2514/1.38845

[28] Gordnier, R. E., Kumar Chimakurthi, S., Cesnik, C. E., and Attar, P. J., "High-Fidelity Aeroelastic Computations of a Flapping Wing with Spanwise Flexibility," *Journal of Fluids and Structures*, Vol. 40, No. 7, 2013, pp. 86–104.
doi:10.1016/j.jfluidstructs.2013.03.009

[29] Alonso, J. J., and Jameson, A., "Fully-Implicit Time-Marching Aeroelastic Solutions," AIAA Paper 1994-0056, Jan. 1994.

[30] Lifante, C., Frank, T., and Kuntz, M., "Extension and Validation of the CFX Cavitation Model for Sheet and Tip Vortex Cavitation on Hydrofoils," *Fifth Joint FZR and ANSYS Workshop*, Multiphase Flows: Simulation, Experiment and Application, ANSYS, Darmstadt, 2007, pp. 1–30.

[31] Nicolato, P. C., and Moreira, R. M., "Numerical Modeling of Water Wave Impact on Reservoirs," *Proceedings of the 20th International Congress of Mechanical Engineering*, Associação Brasileira de Engenharia e Ciências Mecânicas–ABCM, Brazil, 2009, pp. 1–9.

[32] Scott, D., Sabourin, M., Beaulieu, S., Papillon, B., and Ellis, C., "CFD Model of an Aerating Hydrofoil," *IOP Conference Series: Earth and Environmental Science*, Vol. 22, No. 6, 2014, Paper 062008.

[33] Young, J., "Numerical Simulation of the Unsteady Aerodynamics of Flapping Airfoils," Ph.D. Thesis, Univ. of New South Wales, Sydney, NSW, Australia, 2005.

[34] Zhu, Q., "Optimal Frequency for Flow Energy Harvesting of a Flapping Foil," *Journal of Fluid Mechanics*, Vol. 675, No. 20, 2011, pp. 495–517.
doi:10.1017/S0022112011000334

[35] Katz, J., and Weihs, D., "Hydrodynamic Propulsion by Large Amplitude Oscillation of an Airfoil with Chordwise Flexibility," *Journal of Fluid Mechanics*, Vol. 88, No. 3, 1978, pp. 485–497.
doi:10.1017/S0022112078002220

[36] Katz, J., and Weihs, D., "Large Amplitude Unsteady Motion of a Flexible Slender Propulsor," *Journal of Fluid Mechanics*, Vol. 90, No. 4, 1979, pp. 713–723.
doi:10.1017/S0022112079002494

R. Gordnier
Associate Editor